

Numerical and experimental studies on impact sound radiated by rib-stiffened plates

Pengchao Wang¹
Cédric Van hoorickx²
Geert Lombaert³
Edwin Reynders⁴

KU Leuven, Department of Civil Engineering, Structural Mechanics Section
Kasteelpark Arenberg 40, Box 2448, 3001 Leuven, Belgium

ABSTRACT

Rib-stiffened plates are widely applied in civil engineering as they achieve a similar static stiffness as plain plates with a substantially lower weight. Unfortunately, this generally leads to a reduced impact sound insulation. The quantitative assessment of the impact sound insulation of rib-stiffened plates is complex for most of the acoustic frequency range. At the frequencies where the wavelength of deformation is much larger than the stiffener spacing, the stiffeners induced orthotropy leads to an increased width of the coincidence zone. At high frequencies, the point impedance is much larger at the ribs than in between them. This work aims at gaining insight in the impact sound radiation performance of rib-stiffened plates. To this end, a dedicated impact sound computation model is proposed. A finite element model of a rib-stiffened PMMA plate is constructed, in which the mechanical properties are calibrated using experimentally obtained modal characteristics. This model is coupled to a diffuse model of an adjacent room, and the predicted impact sound radiation is validated by measurements. Finally, the effect of adding stiffeners is numerically investigated by comparing the sound radiation efficiency, vibration level, and impact sound radiation of the rib-stiffened plate and simulated plane PMMA plates with equivalent static stiffnesses.

Keywords: Impact sound radiation, rib-stiffened plate, model calibration

I-INCE Classification of Subject Number: 42

¹email: pengchao.wang@kuleuven.be

²email: cedric.vanhoorickx@kuleuven.be

³email: geert.lombaert@kuleuven.be

⁴email: edwin.reynders@kuleuven.be

1. INTRODUCTION

Rib-stiffened plates are widely applied in civil engineering as they achieve an equivalent static stiffness as plain plates with a lower weight. Unfortunately, it is challenging for rib-stiffened plates to achieve impact sound insulation that is as good as heavyweight plane plates.

The quantitative assessment of the impact sound insulation of rib-stiffened plates is complex at a wide frequency range. The stiffeners induce orthotropy to the isotropic plates [1]. At lower frequencies where the structural wavelength is much larger than the stiffener spacing, the additional bending stiffness of the discrete stiffeners is considered as uniformly averaged over the plate surface [2]. The sound radiation is characterized by a coincidence zone that is bounded by two coincidence frequencies. The lower and higher coincidence frequencies are related to the structural wavelength in the stiffened and unstiffened directions, respectively [3]. At frequencies where the structural wavelength is much smaller than the stiffener spacing, the inter-stiffener parts of the plate are considered as small individual panels. The sound radiation efficiency of the entire plate, contributed by the regions along the edges of the individual panels, is much higher than the one of the unstiffened plate [4]. The impact sound radiation at high frequencies depends also on the impact locations, since the driving point impedance is much larger above the ribs than in between them.

A series of studies has been performed on the impact sound radiation of periodical rib-stiffened structures. Mejdí and Atalla [5] performed a semi-analytical model to compute the point force induced sound radiation by rib-stiffened plates. Legault et al. [6] developed a periodic model to compute the impact sound radiated by stiffened structures, assumed as infinitely expanded. Fu et al. [7] analytically analyzed the influences of modal coupling terms, boundary conditions, and stiffener spacing on the point force induced sound radiation by ribbed plates. The vibro-acoustic analysis of rib-stiffened structures has also been numerically performed using the finite element (FE) method [8, 9], the boundary element method [10], the transfer matrix method [11], etc. Nevertheless, the vibro-acoustic analysis of the rib-stiffened structures remains challenging.

The aim of this work is to study the impact sound radiated by rib-stiffened plates into adjacent acoustic fields, both numerically and experimentally. The outline of the paper is as follows. Section 2 introduces a numerical model to compute the impact sound radiated by plates. Next, section 3 describes the FE model of the considered rib-stiffened polymethyl methacrylate (PMMA) plate, of which the mechanical properties and boundary conditions were of special concern. Section 4 performs an experimental validation of the computed impact sound radiation. In section 5, the rib-stiffened plate was additionally modeled as an orthotropic plane plate to determine the equivalent bending stiffnesses in different directions. The sound radiation efficiency, vibration level and impact sound radiation of the rib-stiffened plate are compared to the ones of numerically modeled plane PMMA plates with comparable bending stiffnesses. Finally, section 6 concludes the work.

2. IMPACT SOUND COMPUTATION MODEL

This section describes an approach to compute the impact sound radiated by a plate into an adjacent room. A wide frequency range is considered, e.g., from 50 Hz to 4000 Hz. The structural vibration of the plate is computed in full detail using the FE method. Using

an FE model of the room at middle and high frequencies is computationally expensive, since a large number of degrees of freedom (DOFs) are needed to compute the short-wavelength deformation [12]. Moreover, as the room acoustic field is sensitive to small wave scattering elements [13], the acoustic response computed by a deterministic system loses its meaning. In this work, the local room geometry and configuration are assumed as highly uncertain, and the room is modeled as a pure-tone diffuse field. The equation of the motion for the plate, that is discretized by the FE method, is written as

$$\mathbf{D}_s \hat{\mathbf{u}} = \hat{\mathbf{f}}, \quad (1)$$

where $\hat{\mathbf{u}}$ and $\hat{\mathbf{f}} \in \mathbb{C}^{n_{\text{dof}}}$ are the displacement and excitation force vectors, with n_{dof} the number of structural DOFs. $\mathbf{D}_s \in \mathbb{C}^{n_{\text{dof}} \times n_{\text{dof}}}$ is the structural dynamic stiffness matrix. At any angular frequency ω , the structural displacement at an arbitrary coordinate \mathbf{x} due to an excitation at \mathbf{x}_0 can be computed by means of modal decomposition:

$$\hat{u}(\omega, \mathbf{x}) = \sum_{j=1}^{N_m} \frac{\phi_j(\mathbf{x})\phi_j(\mathbf{x}_0)\hat{f}(\mathbf{x}_0)}{-\omega^2 + \omega_j^2 + i\eta_s\omega\omega_j}, \quad (2)$$

where $\phi_j \in \mathbb{R}^{n_{\text{dof}}}$ and ω_j are the mode shape and angular natural frequency of the structural mode j , N_m is the number of structural modes that are considered to contribute the structural response, and η_s is the structural damping loss factor. The sound power radiated by an infinitely baffled plate into an adjacent direct field is given by

$$P_{\text{rad}} = \frac{\omega}{2} \text{Im}\{\hat{\mathbf{u}}^H(\omega)\mathbf{D}_{\text{dir}}\hat{\mathbf{u}}(\omega)\}, \quad (3)$$

in which $\mathbf{D}_{\text{dir}} \in \mathbb{C}^{n_{\text{dof}} \times n_{\text{dof}}}$ is the dynamic stiffness matrix of the direct field, as seen from the plate-room interface [14]. The notation $(\cdot)^H$ denotes the Hermitian transpose, i.e., $\hat{\mathbf{u}}^H = \hat{\mathbf{u}}^{*T}$. The power P_{rad} in the direct field flows into the diffuse field of the room and dissipated, such that

$$P_{\text{rad}} = P_{\text{diss}}, \quad (4)$$

where P_{diss} is the power dissipated in the diffuse field. At any angular frequency ω , the dissipated power P_{diss} in the diffuse field is expressed as

$$P_{\text{diss}} = \omega\eta_a\hat{E}_a, \quad (5)$$

in which η_a is the damping loss factor of the room, and \hat{E}_a is the sound energy in the room. Using Equations 3 to 5, the sound energy \hat{E}_a in the room is easily computed. The normalized impact sound pressure level in the room equals

$$L_n = 10 \log \frac{\hat{E}_a \rho_0 c^2}{V p_0^2} + 10 \log \frac{A}{A_0}, \quad (6)$$

where A is the absorption area in the room, and $p_0 = 2 \times 10^{-5}$ Pa and $A_0 = 10 \text{ m}^2$ are the reference sound pressure and the reference absorption area, respectively. The absorption area A is computed using Sabine's formula:

$$A = \frac{0.16V}{T_a}, \quad (7)$$

in which V and T_a are the reverberation time and the volume of the room.

3. FE MODEL OF A RIB-STIFFENED PMMA PLATE

Figure 1 shows the rib-stiffened PMMA plate considered in this work, which is mounted in a small vertical opening in the KU Leuven Acoustics Laboratory. The room at each side of opening has a volume of $V = 87 \text{ m}^3$. Figure 2 displays the geometry of the rib-stiffened plate. The base plate has a width of $L_x = 1.235 \text{ m}$, a height of $L_y = 1.485 \text{ m}$, and a thickness of $t_p = 15 \text{ mm}$. The base plate is attached to 11 steel L30 stiffeners, which have an outer leg length of $L_s = 30 \text{ mm}$ and a thickness of $t_s = 3 \text{ mm}$. The center-to-center spacing between the stiffeners is $d_x = 100 \text{ mm}$. The distance between a vertical edge of the plate and the closest vertical edge of the stiffeners is $a_x = 102.5 \text{ mm}$, and the distance between a horizontal edge of the plate and the closest end section of a stiffener is $a_y = 52.5 \text{ mm}$. Each stiffener is glued to the base plate over the entire contact surface, and additionally screwed to the base plate at four points [15].



Figure 1: The plate mounted in the small vertical transmission opening of the KU Leuven Acoustics Laboratory.

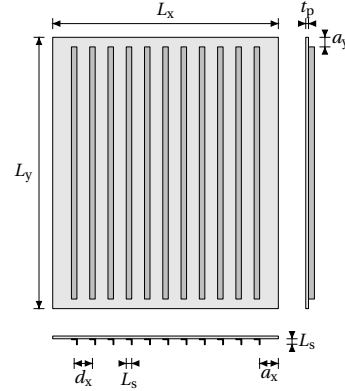


Figure 2: Geometry of the rib-stiffened PMMA plate (front, top, and side view).

Sections 3.1 and 3.2 describe two essential steps of constructing a FE model for the plate: the calibration of the mechanical properties, and the determination of the boundary conditions in the laboratory setup in figure 1. Both steps were performed based on the experimentally identified mode shapes and natural frequencies of the plate in different measurement setups.

3.1. Calibration of mechanical properties

A dynamic test was performed on this plate in order to identify its bending mode shapes and natural frequencies. Figure 3 illustrates the measurement setup, in which the plate was freely suspended by ropes to approximate free-free boundary conditions. The plate was perpendicularly excited by a hammer at a corner, and the out-of-plane acceleration was measured by accelerometers at a total of 35 positions in two individual accelerometer setups. A sampling frequency of 1000 Hz was used.

An acceleration-based modal analysis for each beam was performed using MACEC, a Matlab toolbox for experimental and operational modal analysis [16]. The Combined deterministic-stochastic Subspace Identification (CSI) algorithm [17] was applied, in which both the input force and the output acceleration data were used for the identification. Figures 4 shows the mode shapes and natural frequencies of 10 identified out-of-plane bending modes.

A FE model of the rib-stiffened plate was constructed in ANSYS. Both the base plate and the stiffeners were modeled with four-node linear shell elements (of the SHELL181

type). The base plate and the stiffeners were rigidly connected over their contact surfaces, and free-free boundary conditions were assumed in the model. Next, the mechanical properties of the plate were estimated by a model calibration process, in which the identified eigenmodes shown in Figure 4 were compared with the ones computed by the FE model. The Young's moduli of the base plate and the stiffeners, E_p and E_s , and the Poisson's ratio of the base plate ν_p were chosen as calibration parameters. The Poisson's ratio of the stiffeners, and the densities of the base plate and the stiffeners were taken as $\nu_s = 0.3$, $\rho_p = 1170 \text{ kg/m}^3$, and $\rho_s = 7850 \text{ kg/m}^3$, respectively.

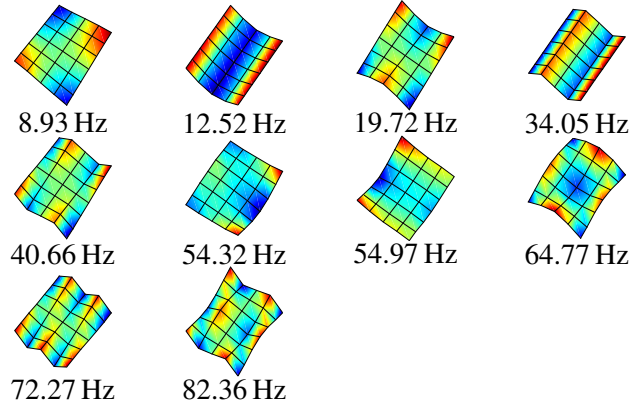


Figure 3: Measurement setup of the dynamic test on the plate with free-free boundary conditions. Figure 4: Mode shapes and natural frequencies of the plate with free-free boundary conditions.

Calibration parameters were updated by minimizing the sum of squared distances d_j between each identified mode j and the closest computed mode. The distance d_j is given as a function of E_p , E_s , and ν_p :

$$d_j(E_p, E_s, \nu_p) = \frac{|f_{id,j} - f_{c,j}(E_p, E_s, \nu_p)|}{\max(f_{id,j}, f_{c,j}(E_p, E_s, \nu_p))} + 1 - \text{MAC}(\phi_{id,j}, \phi_{c,j}(E_p, E_s, \nu_p)), \quad (8)$$

in which the subscripts 'id' and 'c' indicates identified and computed values, respectively. The modal assurance criterion (MAC) [18] measures the degrees of correspondence between the identified and computed mode shapes:

$$\text{MAC}(\phi_{id,j}, \phi_{c,j}(E_p, E_s, \nu_p)) = \frac{|\phi_{id,j}^T \phi_{c,j}(E_p, E_s, \nu_p)|^2}{\|\phi_{id,j}\|^2 \|\phi_{c,j}(E_p, E_s, \nu_p)\|^2}. \quad (9)$$

A MAC value close to unity indicates perfect correspondence of the mode shapes, while a significantly lower value indicates linear independence of mode shapes. An objective function is then defined as the sum of squared distances for modes 1 to 10:

$$f_{\text{obj}}(E_p, E_s, \nu_p) = \sum_{j=1}^{10} d_j^2(E_p, E_s, \nu_p). \quad (10)$$

The minimization of $f_{\text{obj}}(E_p, E_s, \nu_p)$ is a nonlinear least-squares problem that was numerically solved by an iterative, trust-region-reflective Newton method in Matlab (*lsqnonlin* routine with a tolerance of 10^{-5} on the three calibration parameters and the objective function $f_{\text{obj}}(E_p, E_s, \nu_p)$) [15]. In each iteration, the mode shapes and natural frequencies were computed by the FE model, using the temporarily updated

values of the three calibration parameters. During the calibration, the values of the three calibration parameters were taken from realistic ranges of $0.5 \text{ GPa} \leq E_p \leq 10 \text{ GPa}$, $50 \text{ GPa} \leq E_s \leq 300 \text{ GPa}$, and $0.3 \leq \nu_p \leq 0.45$. The optimized results are $E_p = 1.65 \text{ GPa}$, $E_s = 209.53 \text{ GPa}$, and $\nu_p = 0.38$, and the corresponding value of the objective function in Equation 10 is 0.047. Figure 5 shows the relative differences of mode shapes and natural frequencies, which indicate good correspondence between the identified and computed modal results.

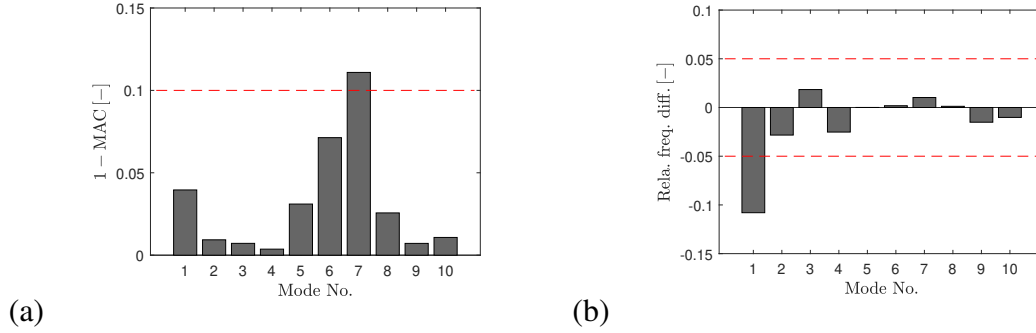


Figure 5: Relative differences of (a) mode shapes (measured as $1 - \text{MAC}$) and (b) natural frequencies between 10 identified and computed modes of the plate with free-free boundary conditions.

3.2. Determination of boundary conditions

To gain an insight in the boundary conditions of the plate in the laboratory step (figure 1), a roving hammer test was performed, during which the plate was excited with an impact hammer at 63 different positions, and the acceleration was measured with accelerometers at nine fixed positions. A sampling frequency of 1000 Hz was used. The experimental data was processed, during which a frequency response function (FRF) matrix between the hammer and accelerometer locations was computed using the H_1 estimator [19, p.141]. Next, a parametric right matrix fraction description model was fitted to the FRF matrix using the poly-reference least squares complex frequency domain (pLSCF) method [20, 21]. Finally, modes were selected from a stabilized diagram. Figure 6 displays the mode shapes and natural frequencies of eight identified out-of-plane bending modes of the mounted plate.

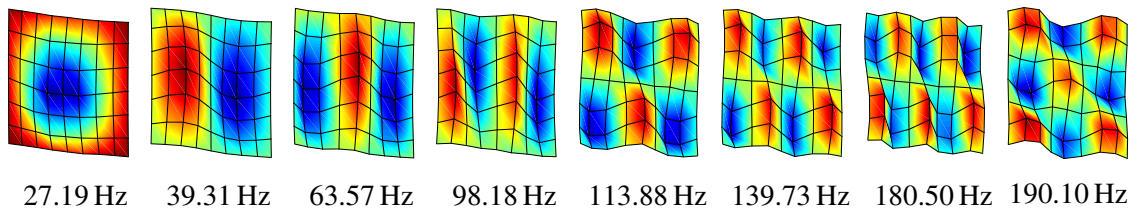


Figure 6: Mode shapes and natural frequencies of 8 identified out-of-plane bending modes of the mounted plate.

In the FE model, the translations along the bottom edge of the plate were fixed, assuming that this edge is greatly restrained by the opening. For the other three edges, only the out-of-plane translations were restrained. Figure 7 displays the relative

differences of mode shapes and natural frequencies between the eight identified modes (in figure 6) and the modes computed with the FE model. As good correspondence between the identified and computed modes are achieved, these conditions are applied in the remainder of the work.

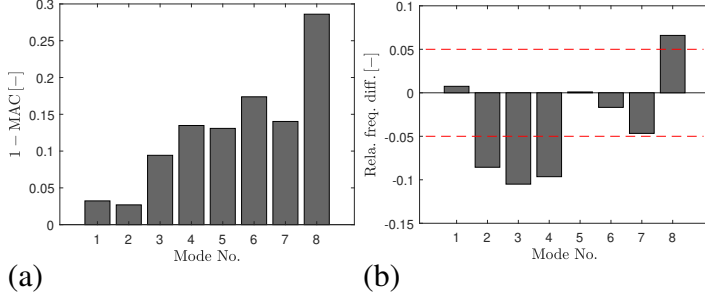


Figure 7: Relative differences of (a) mode shapes (measured as $1 - \text{MAC}$) and (b) natural frequencies between eight identified and computed modes of the mounted plate.

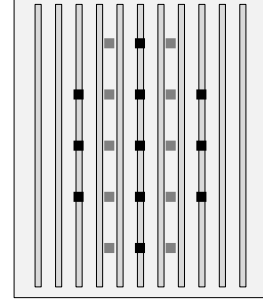


Figure 8: 11 rib impact positions and 10 inter-rib impact positions in the impact sound radiation measurement.

4. EXPERIMENTAL VALIDATION

In this section, the computed impact sound radiation is discussed and experimentally validated. Section 4.1 describes the measurement setups of an impact sound radiation test and a structural reverberation test. Section 4.2 discusses the validation of the computed sound pressure levels.

4.1. Measurement setup

In the impact sound radiation test, the plate was excited using an instrumented hammer at 11 positions above the stiffeners and 10 positions between the stiffeners, which are indicated as ‘rib positions’ and ‘inter-rib positions’, respectively. The impact positions are shown in figure 8. For each impact position, repetitive impacts were given for a period of 40 s, and the input hammer force signal was acquired. The resulting sound pressure levels were sampled at eight microphone positions in the central zone of the receiving room.

A structural reverberation test was also performed to determine the structural damping η_s . Single impulse excitations were given by a hammer at 20 positions in the central part of the plate, and the resulting acceleration was acquired by accelerometers at 15 positions. The structural reverberation time T_s , corresponding to the decay of the vibration level by 60 dB after an impulse excitation on the structure, is evaluated using an integrated impulse response method in ISO-3382 [22]. The structural damping loss factor at an angular frequency ω is computed by

$$\eta_s = \frac{4.4\pi}{\omega T_s}. \quad (11)$$

In addition, to compute the sound pressure levels in the room using Eqs. (5) to (6), the values of the acoustic reverberation time, the sound speed, and the air density are taken

as $T_a = 1.5$ s, $c = 343$ m/s, and $\rho_0 = 1.2$ kg/m³, respectively. The acoustic damping loss factor at an angular frequency ω is computed by

$$\eta_a = \frac{4.4\pi}{\omega T_a}. \quad (12)$$

4.2. Validation of computed sound pressure levels

Figure 10 displays the power spectrum densities (PSDs) of the impact force spectra for the hammer excitation on 11 rib positions and 10 inter-rib positions. The impact forces applied at different impact positions were of the same magnitude. Figure 11 shows the measured and computed normalized harmonic sound pressure levels in the receiving room that are averaged over excitations at 11 rib and 10 inter-rib positions, respectively. The results are computed for the experimental hammer impact forces. The measured results are also averaged over microphone positions in the room.

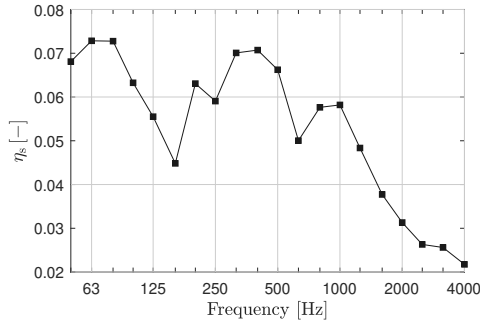


Figure 9: Damping loss factor of the plate estimated by the structural reverberation time test.

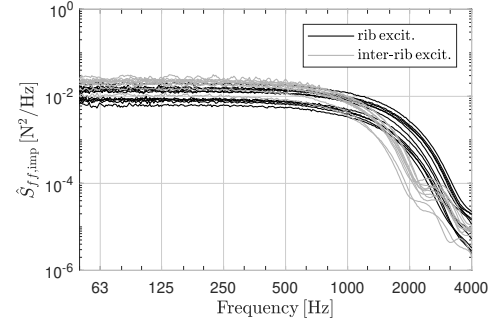
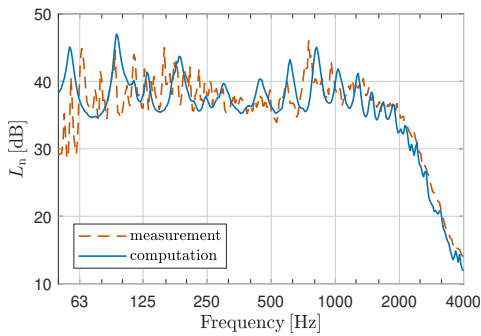
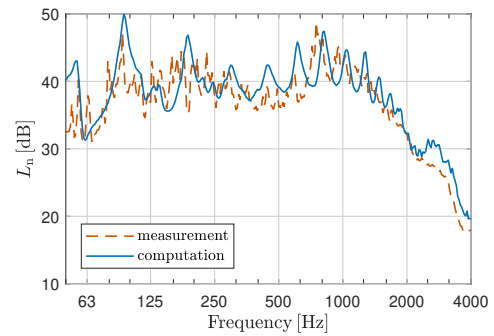


Figure 10: Measured PSDs of the impact force spectra for hammer excitations on 11 rib positions and 10 inter-rib positions. Each curve is averaged over the microphone setups.



(a)



(b)

Figure 11: Measured and computed normalized harmonic sound pressure levels in the receiving room that are averaged over excitations at (a) 11 rib positions and (b) 10 inter-rib positions of the plate. The results are computed for the experimental hammer impact force. The measured results are also averaged over the microphone positions in the room.

Good correspondences of the magnitudes between the measured and computed results are generally achieved. At low frequencies from 50 Hz to 200 Hz, the acoustic response is dominated by the acoustic modes that are disregarded by the diffuse field

model. Therefore, the computed results only display structural resonances, while the acoustic resonant peaks are absent. At frequencies above 200 Hz, the measured results are well captured by the computed results, as the room is considered as a diffuse field, which fulfills the SEA assumption. The minor discrepancies between the measured and computed results can be attributed to the limited accuracies of the FE model, the structural and acoustic damping, the measurement errors, etc.

5. NUMERICAL INVESTIGATION

This section investigates the influence of stiffeners to the impact sound radiation of the plates at different frequency ranges. For this aim, the sound radiation efficiency, vibration level, and impact sound radiation of the rib-stiffened plate are compared to the ones of the plane PMMA plates with comparable bending stiffnesses.

First, in order to determine its equivalent bending stiffnesses in different directions, the rib-stiffened plate was modeled as an orthotropic plane plate. This model was constructed in ANSYS using SHELL181 element. The plate thickness was kept as 15 mm, such that the equivalent density is $\rho_{p,eq} = 1911 \text{ kg/m}^3$. The major and minor Poisson's ratios were taken as $\nu_{xy} = 0$ and $\nu_{yx} = 0$, since the effect of the transverse contraction was assumed to be negligible, respecting the shear stiffness [23, p.368-369]. The Young's moduli in the horizontal and vertical directions, and the shear modulus are $E_x = 2.74 \text{ GPa}$, $E_y = 118.14 \text{ GPa}$, and $G_{xy} = 1.76 \text{ GPa}$, which were using a similar model calibration process as described in Section 3.1. The bending stiffnesses in the horizontal and vertical directions, and the effective bending stiffness are then approximated by

$$B_x = \frac{E_x t_p^3}{12(1 - \nu_{xy}\nu_{yx})} \quad (13)$$

$$B_y = \frac{E_y t_p^3}{12(1 - \nu_{yx}\nu_{xy})} \quad (14)$$

$$B_{eff} = \sqrt{B_x B_y}. \quad (15)$$

Next, two FE models were constructed in ANSYS for two plates with the same isotropic properties, width and height as the base plate of the rib-stiffened plate. To achieve the effective bending stiffness and the bending stiffness in the stiffened direction, two plates have thicknesses of 32 mm and 60 mm, and their weights are 30% and 140% higher than that of the rib-stiffened plate, respectively. The computed thin plate limit frequencies [24, Equation 2.92] for these two plates are both lower than 2000 Hz, therefore the two plates were modeled using 3D eight-node linear solid elements (of the SOLID45 type). The boundary conditions of each plane plate were defined in the same way as for the rib-stiffened plate, such that the bottom edge was clamped, and the out-of-plane translations along the other three edges were restrained.

Figure 12 displays the sound radiation efficiencies, the velocity levels, and the normalized harmonic sound pressure levels in the adjacent receiving rooms for the rib-stiffened plate, the 32 mm-thick and 60 mm-thick plane plates, respectively. The sound radiation efficiencies are computed using a modal summation approach [25]. The velocity level is computed by

$$L_v = 10 \log \frac{\langle \hat{v}^2 \rangle_s}{v_0^2}, \quad (16)$$

where $\langle \hat{v}^2 \rangle_s$ is the spatially averaged squared velocity, and $v_0 = 5 \times 10^{-8}$ m/s is the reference velocity specified in NBN EN ISO-1683 [26]. Both the velocity and sound pressure levels are averaged over excitations on 11 rib positions and 10 inter-rib positions for the rib-stiffened plate, respectively. For each of the plane plates, the results are averaged over all 21 positions that were used for the rib-stiffened plate. The PSD of the impact force at each impact position is $1 \text{ N}^2/\text{Hz}$.

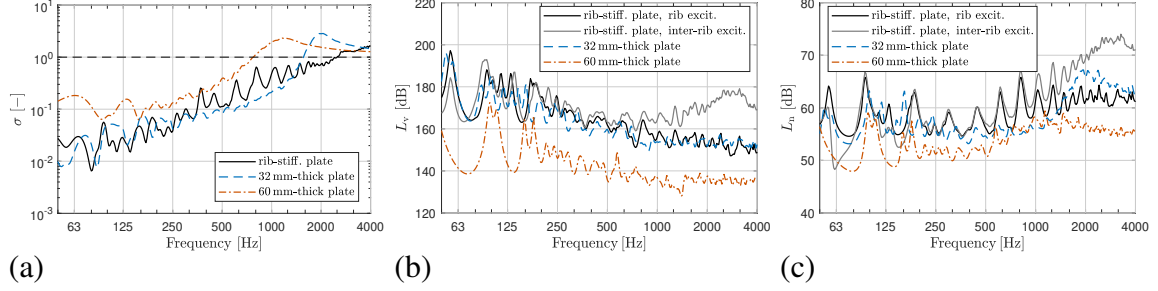


Figure 12: (a) Sound radiation efficiencies, (b) velocity levels, and (c) normalized harmonic sound pressure levels in the adjacent receiving rooms for the rib-stiffened plate, the 32 mm-thick and 60 mm-thick plane plates, respectively. In (b) and (c), the results for the rib-stiffened plate are averaged over 11 rib positions and 10 inter-rib positions, while the results for each of the plane plates are averaged over all 21 positions. The PSD of the impact force at each impact position is $1 \text{ N}^2/\text{Hz}$.

The 60 mm-thick plate has the lowest critical frequency among the three plates, which induces the highest radiation efficiency at a wide frequency range. However, as its velocity level is considerably lower than the other two plates, the resulting sound pressure level is also the lowest among the three plate.

At frequencies above 1600 Hz, the impedance of the rib-stiffened plate above the rib positions is much higher than at the inter-rib positions. Therefore, for this frequency range, the rib excitations induce much lower velocity levels and sound pressure levels than the inter-rib excitations.

On the other hand, at frequencies below 550 Hz, the rib-stiffened plate behaves as an orthotropic plate with an effective bending stiffness B_{eff} ; its radiation efficiency is therefore very close to that of the 32 mm-thick plate. From 550 Hz on, the radiation efficiency of the rib-stiffened plate displays several peaks, corresponding to the coincidence frequencies at which that the bending wavelengths in the vertical direction of the plate modes are equal to the acoustic wavelengths at specific propagating directions. These peaks in the radiation efficiency result in higher sound pressure levels for the rib-stiffened plate at these frequencies.

6. CONCLUSION

This work presents a numerical and experimental study on the impact sound radiation by a rib-stiffened PMMA plate. The vibration of the plate and the resulting sound radiation are deterministically computed by an FE model of the plate, and the sound pressure level in the receiving room is computed by a diffuse room model. The mechanical properties and the boundary conditions of the plate were determined using the experimentally identified eigenmodes of the plate in different measurement setups. The computed impact sound radiation due to hammer excitations on the plate is

experimentally validated. A numerical study shows that, at high frequencies, the driving point impedance is much larger at the ribs than in between them. Therefore, the rib excitations induce much lower structural vibration and impact sound radiation than the inter-rib excitations. Moreover, the low frequency sound radiation efficiency, vibration level and impact sound radiation of a rib-stiffened plate is comparable to an isotropic plane plate with a higher weight and a similar effective bending stiffness.

7. REFERENCES

- [1] M. Heckl. Untersuchungen an orthotropen Platten. *Acustica*, 10:109–115, 1960.
- [2] F. Fahy and P. Gardonio. *Sound and structural vibration: radiation, transmission and response*. Academic Press, Oxford, UK, 2nd edition, 2007.
- [3] A. Santoni, S. Schoenwald, P. Fausti, and H.M. Tröbs. Modelling the radiation efficiency of orthotropic cross-laminated timber plates with simply-supported boundaries. *Applied Acoustics*, 143:112–124, 2019.
- [4] G. Maidanik. Response of ribbed panels to reverberant acoustic fields. *Journal of the Acoustical Society of America*, 34(6):809–826, 1962.
- [5] A. Mejdi and N. Atalla. Dynamic and acoustic response of bidirectionally stiffened plates with eccentric stiffeners subject to airborne and structure-borne excitations. *Journal of Sound and Vibration*, 329:4422–4439, 2010.
- [6] J. Legault, A. Mejdi, and N. Atalla. Vibro-acoustic response of orthogonally stiffened panels: the effects of finite dimensions. *Journal of Sound and Vibration*, 330(24):5928–5948, 2011.
- [7] T. Fu, Z. Chen, H. Yu, C. Li, and X. Liu. An analytical study of the vibroacoustic response of a ribbed plate. *Aerospace Science and Technology*, 73:96–104, 2018.
- [8] D.W. Fox and V.G. Sigillito. Bounds for eigenfrequencies of a plate with an elastically attached reinforcing rib. *International Journal of Solids and Structures*, 18(3):235–247, 1982.
- [9] M. Barrette, A. Berry, and O. Beslin. Vibration of stiffened plates using hierarchical trigonometric functions. *Journal of Sound and Vibration*, 235(5):727–747, 2000.
- [10] E.J. Sapountzakis and Katsikadelis J.T. Dynamic analysis of elastic plates reinforced with beams of doubly-symmetrical cross section. *Computational Mechanics*, 23:430–439, 1999.
- [11] Y. Yong and Y.K. Lin. Propagation of decaying waves in periodic and piecewise periodic structures of finite length. *Journal of Sound and Vibration*, 129(2):99–118, 1989.
- [12] R. S. Langley and P. Bremner. A hybrid method for the vibration analysis of complex structural-acoustic systems. *Journal of the Acoustical Society of America*, 105(3):1657–1671, 1999.

- [13] J.B. Robert. The limits of predictability due to manufacturing and environmentally induced uncertainty. In *Proceedings of Inter-Noise 96, the 1996 International Congress on Noise Control Engineering*, pages 2867–2872, Liverpool, UK, July–August 1996.
- [14] R.S. Langley and V. Cotoni. Response variance prediction for uncertain vibro-acoustic systems using a hybrid deterministic-statistical method. *Journal of the Acoustical Society of America*, 122(6):3445–3463, 2007.
- [15] E. Reynders, C. Van hoorickx, and A. Dijckmans. Sound transmission through finite rib-stiffened and orthotropic plates. *Acta Acustica united with Acustica*, 102(6):999–1010, 2016.
- [16] E. Reynders, M. Schevenels, and G. De Roeck. MACEC: A Matlab toolbox for experimental and operational analysis. Report BWM-2008-07, Department of Civil Engineering, KU Leuven, April 2008.
- [17] E. Reynders and G. De Roeck. Reference-based combined deterministic-stochastic subspace identification for experimental and operational modal analysis. *Mechanical Systems and Signal Processing*, 22(3):617–637, 2008.
- [18] R.J. Allemang and D.L. Brown. A correlation coefficient for modal vector analysis. In *Proceedings of the 1st International Modal Analysis Conference*, pages 110–116, Orlando, FL, 1982.
- [19] D. J. Ewins. *Modal testing*. Research Studies Press, Baldock, U.K., second edition, 2000.
- [20] P. Guillaume, P. Verboven, S. Vanlanduit, H. Van der Auweraer, and B. Peeters. A poly-reference implementation of the least-squares complex frequency domain-estimator. In *Proceedings of the 21th International Modal Analysis Conference*, Kissimmee, FL, February 2003.
- [21] E. Reynders. System identification methods for (operational) modal analysis: review and comparison. *Archives of Computational Methods in Engineering*, 19(1):51–124, 2012.
- [22] International Organization for Standardization. *ISO 3382:1997: Acoustics - Measurement of the reverberation time of rooms with reference to other acoustical parameters*, 1997.
- [23] S. Timoshenko and S. Woinowsky-Krieger. *Theory of plates and shells*. McGraw-Hill, New York, U.S.A., second edition, 1959.
- [24] C. Hopkins. *Sound insulation*. Elsevier Ltd., Oxford, 2007.
- [25] G. Xie, D.J. Thompson, and C.J.C. Jones. The radiation efficiency of baffled plates and strips. *Journal of Sound and Vibration*, 280:181–209, 2005.
- [26] Belgisch Instituut voor Normalisatie. *NBN EN ISO 1683:2015: Acoustics - Preferred reference values for acoustical and vibratory levels*, 2015.